

Deep Learning for 2D grapevine bud detection

Wenceslao Villegas Marset^{a,*}, Diego Sebastián Pérez^a, Carlos Ariel Diaz^a,
Facundo Bromberg^{a,b}

^aUniversidad Tecnológica Nacional, Facultad Regional Mendoza, Grupo de Inteligencia Artificial DHARMA, Dpto. de Sistemas de la Información. Rodríguez 273, CP 5500, Mendoza, Argentina.

^bConsejo Nacional de Investigaciones Científicas y Técnicas (CONICET).

Abstract

Visual inspection is a necessary task to measure relevant variables in viticulture susceptible to automation with computer vision methods. Bud detection is central for various of these tasks such as: measurement of bud sunlight exposure, autonomous pruning, bud counting, type-of-bud classification, bud geometric characterization, internode length, and bud development stage, among others. This paper presents a method for grapevine bud detection based on a *Fully Convolutional Networks Mobile-Net* architecture. To validate its performance, this architecture was compared in the detection task with the known state-of-the-art method for bud detection, showing improvements over three aspects of detection: *segmentation*, *correspondence identification* and *localization*. In its best version of configuration parameters, the present approach showed a detection precision of 95.6%, a detection recall of 93.6%, a mean Dice coefficient of 89.1% for correct detection (i.e., detections whose mask overlaps the true bud) with small and nearby false alarms (i.e., detections not overlapping the true bud) as shown by a mean pixel area of only 8% the area of a true bud, and a distance (between mass centers) of 1.1 true bud diameters. The paper concludes with a discussion of the advantages of our approach for real-world applications.

Keywords: Computer vision, Fully Convolutional Network, Grapevine bud detection, Precision viticulture

*Corresponding author

Email addresses: diego.villegas@alumnos.frm.utn.edu.ar (Wenceslao Villegas Marset), sebastian.perez@frm.utn.edu.ar (Diego Sebastián Pérez), carlos.diaz@frm.utn.edu.ar (Carlos Ariel Diaz), fbromberg@frm.utn.edu.ar (Facundo Bromberg)

1. Introduction

The present work proposes a solution for the autonomous detection of grapevine buds within 2D vineyard images captured in natural field conditions. The proposed approach is based on *Fully Convolutional Networks* (FCN) (Long et al., 2015; Shelhamer et al., 2017), a sort of deep learning model specific for computer vision applications. The present solution contributes to the historical quest for more and better quality information about different vineyard processes that affect both the grapevine productivity and grape quality.

For years, viticulturists have been producing models of the most relevant plant processes (i.e. fruit quality and yield, soil profiling, vine health) and have been gathering a wealth of information to feed into these models. Better and more efficient measuring procedures have resulted in more information, with its corresponding impact on the quality of model outcomes, while inspiring researchers to push the boundaries for producing more sophisticated models. Such information consists of a large set of variables for assessing different aspects of the plant parts involved in these processes: trunks, leaves, berries, buds, shoots, flowers, bunches, and canes. The list of variables is long, i.e.: berry maturity, number, weight, size and volume; cluster compactness, morphology, such as length, width, size, and elongation, as well as cluster volume, number and weight; bud burst, number and size; flower number, leaf area, shoot length, pruning weight, and canopy density, among others (Institute, a,b)).

Nowadays, technology is pushing once again the possibilities regarding the quality and throughput of these measurements with improved digital and autonomous measurement procedures over manual ones. The discipline is experiencing a transition with many of its variables still being measured manually through visual inspection. This results in high labor costs that limit measurement campaigns to only small data samples which, even with the use of statistical inference or spatial interpolation techniques, limit outcome quality (Whelan et al., 1996).

In some cases, this scenario is exacerbated by the need of experts for proper measurement, such as the case of variables associated with the plant phenological stages, such as bud swelling, bud burst, inflorescence, flowering, veraison, and berry ripening, among others (Lorenz et al., 1995); or by a measurement

procedure that requires the destruction of the plant part being measured, which prevents tracking a certain variable over time. Such is the case of the measurement of leaf area, bunch weight, berry weight and pruning weight (Kliewer and Dokoozlian, 2005).

Precision viticulture in general (Bramley, 2009), and computer vision algorithms in particular, have been growing in the last couple of decades, mainly due to their potential for mitigating these limitations (Seng et al., 2018; Matese and Di Gennaro, 2015). These algorithms come along with the promise of an unprecedented boost in the production of vineyard information as well as many expectations not only about possible improvements in the quality of the model’s outcomes, but in its potential to produce better models by feeding all this information to big data algorithms.

The present work contributes to this general endeavor with an algorithm for measuring variables related to one specific plant part: the bud, an organ of major importance as it is the growing point of the fruits, containing all the plant’s productive potential (May, 2000). Our contribution of autonomous bud detection not only enables the autonomous measurement of all bud-related variables currently measured by agronomists (see Table ~1 for a non-exhaustive list of bud-related variables), but it also has the potential to enable the measurement of novel, yet important, variables that at present cannot be measured manually. One example is the total sunlight captured by buds, which depends on the unfeasible manual task of determining the exact location of buds in 3D space. Although the present work focuses on 2D detection, it could be easily upgraded to 3D by, for instance, integrating 2D detection into the workflow proposed by Díaz et al. (2018) (c.f. Section ~1.1 for further details on this workflow).

Table ~1 shows a non-exhaustive list of the main bud-related variables currently measured by vineyard managers (Sánchez and Dokoozlian, 2005; Noyce et al., 2016; Collins et al., 2020), together with an assessment of the extent to which detection contributes to their measurement. The right-most column indicates the information beyond detection necessary to complete the measurement, while the middle columns labeled (i), (ii), and (iii) indicate the specific aspects of detection required for that variable: (i) whether it requires a good *segmentation*, i.e., the discrimination of which pixels in the scene correspond to buds

| Variable | (i) | (ii) | (iii) | |
|-------------------------------------|-----|------|-------|---|
| Bud number | | x | | none |
| Bud area | x | x | | none |
| Type-of-bud classification | x | x | | plant structure (trunk and canes) |
| Bud development stage | x | x | | classifier over bud mask |
| Internode length (by bud detection) | | x | x | plant structure (trunk and canes) |
| Bud volume | | | | 3D reconstruction |
| Bud development monitoring | x | x | x | |
| Incidence of sunlight on the bud | | x | x | 3D reconstruction, leaves 3D superficial geometry |

Table 1: A non-exhaustive list of important bud-related variables accompanied by an assessment of the extent to which detection contributes to their measurement. The right-most column indicates the information beyond detection necessary to complete the measurement, while the middle columns labeled (i), (ii), and (iii) indicate the three aspects of detection required: segmentation, correspondence identification, or localization, respectively.

67 and which correspond to the background (non-bud); ii) a good *correspondence*
68 *identification*, i.e., discrimination of bud pixels as belonging to different buds;
69 or (iii) a good *localization*, i.e., the localization of the bud within the scene.

70 For instance, let us take the *bud number* variable. On the one hand, If it
71 is possible to correctly identify the matches, the bud number coincides directly
72 with the detection count. On the other hand, for the *type-of-bud classification*,
73 in addition to identifying matches, the segmentation of the part of the image
74 corresponding to the bud is necessary to feed a classifier with relevant visual
75 information, minimizing the noise produced by background pixels. Lastly, to
76 measure the *incidence of sunlight on the bud*, segmentation is not necessary, but
77 rather good bud localization, in addition to leaf 3D surface geometry.

78 A good detector, therefore, should be evaluated on all three aspects of seg-
79 mentation, correspondence identification and localization. This is easy for our
80 detector as its implementation first produces a segmentation mask, which is
81 then post-processed to produce correspondence identification and localization.
82 The specific aspects of this approach are detailed in Section ~2. The analysis of
83 detection results presented in Section ~3 shows that this approach is superior to
84 state-of-the-art algorithms for vine bud detection. Finally, Section ~4 discusses
85 the scope, limitations of the results obtained for bud detection, sufficiency of
86 the performance achieved for the measurement of a selection of variables in Ta-
87 ble ~3, as well as the most important conclusions, future work and potential

88 improvements.

89 1.1. Related work

90 A wide variety of research using computer vision and machine learning algo-
91 rithms to acquire information about vineyards (Seng et al., 2018) can be found
92 in the literature, such as berry and bunch detection (Nuske et al., 2011), fruit
93 size and weight estimation (Tardaguila et al., 2012), leaf area indices and yield
94 estimation (Diago et al., 2012), plant phenotyping (Herzog et al., 2014a,b), au-
95 tonomous selective spraying (Berenstein et al., 2010), and more (Tardaguila
96 et al., 2012; Whalley and Shanmuganathan, 2013). Among the outstanding
97 computer algorithms in recent years, *artificial neural networks* have aroused
98 great interest in the industry as a means to carry out various visual recogni-
99 tion tasks (Hirano et al., 2006; Kahng et al., 2017; Tilgner et al., 2019). In
100 particular, *Convolutional Neural Networks* (CNNs) have become the dominant
101 machine learning approach to visual object recognition (Ning et al., 2017). Two
102 recent studies have successfully applied visual recognition techniques based on
103 *deep learning networks* to identify viticultural variables to estimate production
104 in vineyards. One of them Grimm et al. (2019) uses an FCN to carry out seg-
105 mentation of grapevine plant organs such as young shoots, pedicels, flowers,
106 buds or grapes. The other Rudolph et al. (2018) uses images of vines under
107 field conditions that are segmented using a CNN to detect inflorescences, and
108 over these segmented regions, the Circle Hough Transform algorithm is applied
109 to detect flower buds.

110 Several works aim at detecting and locating buds in different types of crops
111 by means of autonomous visual recognition systems. For instance, Tarry et al.
112 (2014) presents an integrated system for chrysanthemum bud detection that can
113 be used to automate labour intensive tasks in floriculture greenhouses. More
114 recently, Zhao et al. (2018) presented a computer vision system used to identify
115 the internodes and buds of stalk crops. To the best of our knowledge and re-
116 search efforts, there are at least four works that specifically address the problem
117 of bud detection in the grapevine by using autonomous visual recognition sys-
118 tems. The research work by Xu et al. (2014), Herzog et al. (2014b) and Pérez
119 et al. (2017) apply different techniques to perform 2D image detection involving
120 different computer and machine learning algorithms. In addition, Díaz et al.

121 (2018) introduces a workflow to localize buds in 3D space. The most relevant
122 details of each are presented below.

123 Xu et al. (2014)’s study presents a bud detection algorithm using indoor
124 captured RGB images and controlled lighting and background conditions specif-
125 ically to establish a groundwork for an autonomous pruning system in winter.
126 The authors apply a threshold filter to discriminate the background of the plant
127 skeleton, resulting in a binary image. They assume that the shape of buds re-
128 sembles corners and apply the *Harris corner detector* algorithm over the binary
129 image to detect them. This process obtains a recall of 0.702, i.e., 70.2% of the
130 buds were detected.

131 Herzog et al. (2014b)’s work presents three methods for bud detection, all
132 of which are semi-automatic and require human intervention to validate the
133 quality of the results. The best result is obtained using an RGB image with
134 an artificial black background and corresponds to a recall of 94%. The authors
135 argue that this recall is enough to solve the problem of phenotyping vines. They
136 also argue that these good results can be explained by the particular green color
137 and the morphology of the already sprouting buds of approximately 2cm.

138 Pérez et al. (2017) outlines an approach for the classification of bud images
139 in winter, using *SVM* as a classifier and *Bag of Features* to compute visual
140 descriptors. They report a recall of over 90% and an accuracy of 86% when
141 sorting images containing at least 60% of a bud and a ratio of 20-80% of bud
142 vs. non-bud pixels. They argue that this classifier can be used in algorithms for
143 2D localization of the *sliding windows* type due to its robustness to variation in
144 window size and position. It is precisely this idea that has been reproduced in
145 the present work to implement the baseline approach based on sliding windows
146 and patch classifier.

147 Finally, Díaz et al. (2018) introduces a workflow for the localization of buds
148 in 3D space. The workflow consists of five steps. The first one reconstructs a 3D
149 point cloud corresponding to the grapevine structure from several RGB images.
150 The second step applies a 2D detection method using a sliding window technique
151 and patch classification. The next step uses a voting scheme to classify each
152 point in the cloud as a bud or non-bud. The fourth step applies the *DBSCAN*
153 clustering algorithm to group points in the cloud that correspond to a bud.

154 Finally, in the fifth step, the localization is performed, obtaining the center of
155 mass coordinates of each 3D point cluster. They report a recall of 45% with an
156 accuracy of 100% and a localization error of approximately 1.5cm , or 3 diameters
157 of bud.

158 Although these research studies represent a great advance in relation to the
159 problem of detecting and localizing buds, they still show at least one of the
160 following limitations (i) use of artificial background outdoors; (ii) controlled
161 lighting indoors; (iii) need for user interaction; (iv) bud detection in very ad-
162 vanced stages of development; (v) low bud detection/classification recall, and
163 (vi) although some of these works perform some kind of segmentation process as
164 part of the approach, none of them aim to segment the bud or report metrics of
165 the quality of the segmentation performed. These limitations represent a major
166 barrier to the effective development of tools for measuring bud-related variables.

167 2. Materials and Methods

168 This section describes the main contribution of the present work, that is,
169 the deep learning setup for 2D image detection of grapevine buds captured in
170 natural conditions. Subsection ~2.1 provides details on the *encoder-decoder*
171 transfer learning architecture and the pre-training chosen for its encoder.

172 The detection results achieved by this approach are contrasted with a bud
173 detection method described in Pérez et al. (2017). In this paper, the authors
174 present a bud/non-bud image classifier and suggest its use for bud detection
175 based on the idea of *sliding windows*. Given an image of a viticultural scene,
176 it subdivides it into a set of *patches* or smaller regions (Pérez et al., 2017) and
177 then detects buds by determining whether or not a certain patch contains a
178 bud by using the image classifier. Our implementation of a detector based on
179 this design is described in Subsection ~2.2. Finally, the section concludes with
180 Subsection ~2.3 that provides details on the training of both methods including
181 details on the image collection used for its training.

182 2.1. Fully Convolutional Network with MobileNet (FCN-MN)

183 As outlined in the introduction, the approach proposes the use of computer
184 vision algorithms to: (i) *segment* buds by *classifying* which pixels in the scene

185 correspond to buds and which pixels correspond to background (non-buds),
186 (ii) *identify bud correspondences* by discriminating those pixels that belong to
187 different buds in the observed scene, and (iii) *localize* each bud in the scene.

188 For the segmentation operation, i.e., pixel classification, the fully convolu-
189 tional network introduced in (Long et al., 2015) is taken as a basis and trained
190 for the specific problem of grapevine bud segmentation. The following section
191 2.1.1 describes in detail the architecture considered for these networks. The re-
192 sulting fully convolutional network returns a probability map on the same scale
193 as the original image, where the value of one pixel represents the probability
194 that the corresponding pixel in the input image belongs to a bud. To obtain a
195 binary mask, a classification threshold of τ is applied to each pixel, classifying
196 the pixel as bud (non-bud) if its probability is higher (lower) than τ . To identify
197 bud correspondences, post-processing of this binary mask is performed to de-
198 termine that two bud pixels correspond to the same bud, as long as they belong
199 to the same connected component, i.e., joined by some sequence of contiguous
200 bud pixels.

201 Finally, there are several alternatives for the localization of objects among
202 which are *bounding box*, *pixel-wise segmentation*, *contour* and *center of mass*
203 of the *object* (Lampert et al., 2008). In this work the last one was considered,
204 choosing to localize buds by the center of mass of the connected component.

205 2.1.1. Encoder-decoder architecture

206 For the pixel classifier, the three versions -32s, 16s and 8s- of the *fully convo-*
207 *lutional networks* originally introduced by Long et al. (2015) were considered for
208 their excellent results in many image segmentation applications (Litjens et al.,
209 2017; Garcia-Garcia et al., 2018; Kaymak and Uçar, 2019). These networks have
210 characteristic architectures with two distinct parts: *encoder* and *decoder* (see
211 Figure ~1).

212 The encoder consists of a convolutional neural network that performs a *down-*
213 *sampling* of an input image into a feature set by means of convolution operations
214 to produce a set of *feature maps*, i.e., an abstract representation of the image
215 that captures semantic and contextual information, but discards fine-grained
216 spatial information. These operations reduce the spatial dimensions of the im-
217 age as one goes deeper into the network, resulting in feature maps 1/n the size

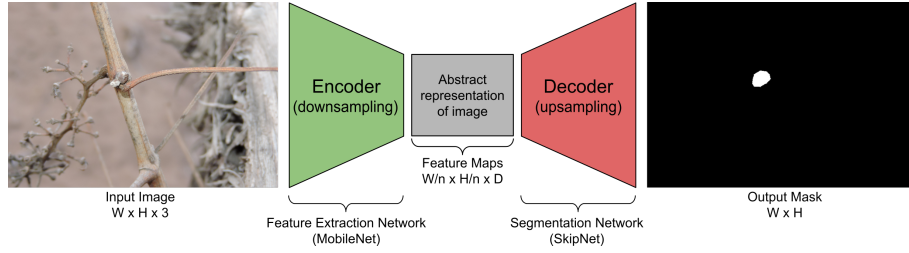


Figure 1: Diagram of the FCN-MN network architecture proposed in this work, based on the FCN proposed by shelhamer2017fully, replacing its feature extraction encoder by MobileNet networks howard2017mobilenets, which produces feature maps with a n downsampling factor. As a decoder for the production of the segmentation map, the SkipNet network siam2018rtseg is used implementing variants 32s, 16s and 8s.

of the input image, where n is the downsampling factor. The decoder is an *upsampling* subnet, which takes the low-resolution feature map set and projects it into pixel space, increasing the resolution to produce a segmentation mask (or dense pixel classification) with the same dimensions as the input image. This operation is implemented as a network of transposed convolutions with trainable parameters, also known as upsampling convolutions (Shelhamer et al., 2017).

On the other hand, to refine segmentation quality, connections that go beyond at least one layer of the network, called *skip connections*, are often used to transfer local spatial information from the internal encoder layers directly to the decoder. In general, these connections improve segmentation results, since they mitigate the loss of spatial information by allowing the decoder to incorporate information from internal feature maps, although their impact may vary depending on the proposed skip architecture. In Long et al. (2015), three skip architectures are proposed: 32s without information from internal encoder layers; 16s that adds spatial information from deep encoder layers; and 8s that adds spatial information from deep and less deep encoder layers. The details of these architectures are beyond the scope of this paper, but can be found in Long et al. (2015) and Shelhamer et al. (2017). Since the results reported in the literature are not conclusive regarding which architecture is better, Long et al. (2015); Shelhamer et al. (2017), in this work all three alternatives are considered.

In spite of having achieved excellent results in practice, these architectures

carry a significant load of computational resources. With this in mind, in this work the VGG encoder [Simonyan and Zisserman \(2015\)](#) originally proposed by Long for FCNs was replaced by the MobileNet network [Howard et al. \(2017\)](#). This network stands out for its only 4.2 million parameters against the 138 million VGG parameters, allowing the training and testing process to be considerably faster, with a much lower memory requirement, but maintaining performance. The use of MobileNet as an encoder in the fully convolutional networks of [Long et al. \(2015\)](#) is not new, but had already been proposed for the 8s architecture by [Siam et al. \(2018\)](#) in his SkipNet architecture. Technically, [Siam et al. \(2018\)](#)'s proposal is extremely simple; that is why we dare extend it to the 16s and 32s architectures originally proposed by [\(Long et al., 2015\)](#). It is due to these changes that for the rest of the paper these networks are referred to as **FCN-MN**.

2.2. *Sliding Windows detector*

This section describes the approach proposed by [Pérez et al. \(2017\)](#) for the classification of bud images and its implementation for detection based on sliding windows described in the original paper. From now on, this detection approach will be referred to as SW. The approach follows three steps: (i) it applies the sliding windows algorithm to an image to extract patches (sub-images or rectangular regions); (ii) it sorts (all pixels of) each patch into bud or non-bud using the algorithm presented in [Pérez et al. \(2017\)](#); and (iii) it produces the final segmentation mask using a voting scheme. Details of each step are provided below.

Sliding windows techniques comprise a family of algorithms widely used in the past as part of various approaches to object localization with bounding boxes ([Divvala et al., 2009](#); [Wang et al., 2009](#); [Chum and Zisserman, 2007](#); [Ferrari et al., 2007](#); [Dalal and Triggs, 2005](#); [Rowley et al., 1996](#)). In these algorithms, each image is scanned densely from one end of the image (e.g. upper left corner) to the other end (e.g. lower right corner) by a rectangular sliding window in different scales and different displacements, extracting sub-images or patches from the original image. In this work, 10 window sizes of equal height and width are defined, namely 100, 200, 300, 400, 500, 600, 700, 800, 900 and 1000 pixels, with a horizontal displacement of 50% the width of the

window and a vertical displacement of 50% the height of the window, resulting
 in a 50% overlap between contiguous patches. These values were chosen on the
 basis of the robustness analysis of the classifier presented by Pérez et al. (2017)
 for the window geometry. This analysis shows that the classifier (explained in
 section 2.3.3) is robust for patches that contain at least 60% of the pixels of a
 bud, and these must cover at least 20% of the patch. If we consider extreme
 cases, i.e., the smallest bud diameter 100px and the largest 1600px, window
 sizes of 100px and 1000px could contain at least 60% of the pixels of a bud.
 In addition, using a 50% displacement, it is guaranteed that at least one patch
 will contain more than 20% bud pixels, 50px and 500px, respectively. The
 authors argue that a sliding window detection algorithm could easily propose a
 scheme for choosing window size and displacement to ensure that at some point
 in the scan the window meets robustness requirements. However, no details
 are given on how to implement it, so in this paper we only report results for
 fixed window sizes and explained displacement. Since the collection buds have
 a variable pixel diameter (corresponding to patches varying from 100×100 to
 1600×1600 pixels, approximately), not all window sizes will be able to satisfy
 the robustness requirements for all patches, but the results can still be useful
 to make a comparison with the FCN-MN approach.

The second step in this approach is to determine whether a patch is a bud or
 non-bud type. The classifier in Pérez et al. (2017) takes the patches produced by
 the sliding windows and, for each patch, it performs the following operations: (i)
 it computes low-level visual features using the *Scale Invariant Feature Transform*
 (SIFT) Lowe (2004) algorithm; (ii) it builds a high-level descriptor for each
 patch using the *Bag of Features* (BoF) Csurka et al. (2004) algorithm on top
 of the SIFT features from the previous step; and (iii) it determines the class
 of each patch using the BoF descriptor on top of a classifier built using the
Support Vectors Machine Vapnik (2013) algorithm. Details of the training of
 this classifier are postponed until Section 2.3.3 (SW training).

Finally, the third step of the approach is to build the binary mask where
 the pixels belonging to the bud and non-bud class are tagged. This mask is
 constructed through a voting scheme where each pixel adds one vote for each
 patch that contains it classified as a bud, which could be a maximum of four

for some pixels, because the proposed displacement between patches has both horizontal and vertical overlap. Then, a minimum voting threshold of ν is established that can take values from 1 to 4, so that pixels with a number of votes equal to or greater than ν are classified as bud; otherwise, they are classified as non-bud.

2.3. Model training

This section provides details of the training process for each approach. In order to contrast both approaches they have been designed to receive the same type of input, i.e., an image of a viticultural scene, and to produce the same outputs, i.e., a binary mask of the same size as the original image whose positive pixels represent bud-type pixels, together with the localization coordinates (X,Y) of these buds. This allows both to be trained with the same image collection, which is described in the following section, followed by model-specific training details.

2.3.1. Image collection

The image collection used in this study is the same collection originally used in Pérez et al. (2017), which has been downloaded from <http://dharm.frm.utn.edu.ar/vise/bc> as indicated by the authors. The complete collection consists of 760 images captured in winter in natural field conditions. However, in this work, only the 698 images containing exactly one bud were taken. Each image is accompanied by the ground truth, that is, a mask with manual segmentation of the bud. These images and their masks were used during the training and evaluation of the detection models. For this purpose, the image collection was separated into two disjoint subsets: the *train set* with 80% of the images and the *test set* with the remaining 20%. This resulted in a train set of 558 images and a test set of 140 images, both with their respective ground truth masks. In this way, the two proposed approaches use exactly the same 558 images during training and the same 140 images during testing.

2.3.2. FCN-MN approach training

The 558 images reserved for this purpose were used to train this approach. These images have different resolutions; however, the three proposed FCN-MNs

require a fixed size entry. Therefore, all images (including their masks) were scaled to a resolution of 1024×1024 pixels using a bilinear interpolation method (Han, 2013). In addition, for the train set images, the pixel RGB intensity values were scaled from $[0.255]$ to $[-1, 1]$.

Given the small number of images in the train set, two techniques widely used in practice were employed to achieve robust training: *transfer learning* Pan and Yang (2009) and *data augmentation* Shorten and Khoshgoftaar (2019). The transfer learning process was carried out as follows: (i) the original MobileNet network proposed by Howard et al. (2017) was implemented; (ii) the network was initialized with the parameters pre-trained on the ImageNet benchmark dataset Kornblith et al. (2019); (iii) the MobileNet multi-class classification layer was replaced by a binary classification layer; (iv) the network was trained as a bud and non-bud patch classifier in an analogous way to SVM training, using the balanced patch train set after scaling all its images to 224×224 pixels; and (v) the parameters obtained in the previous step were used to initialize the encoder of our FCN-MN, introduced in Section 2.1. The data augmentation process was applied on the fly during training, i.e., as the process required new images. For each train set image, 200 new images (111600 in total) were generated by simultaneously applying the following seven operations, whose values were taken at random with uniform probability: *rotation* of up to 45° ; *horizontal shifting* of up to 40%; *vertical shifting* of up to 40%; *shear* of up to 10%; *Zoom* of up to 30%; *horizontal flip* and *vertical flip*.

For the training of the three FCN-MN variants -8s, 16s, and 32s- it is required to specify the *optimization method* and dropout value, two parameters typically defined by the user. In this work, the optimization methods considered were: *Adam* with learning rate parameters= 0.001, $\beta_1 = 0.9$ and $\beta_2 = 0.999$; *RMSProp* with learning rate parameters = 0.001 and $\rho = 0.9$; and *Stochastic Gradient Descent* with learning rate parameters = 0.0001 and $\text{momentum} = 0.9$. For the dropout case, two values were considered: 0.5 and 0.001. These values were pre-selected by preliminary experiments not discussed here.

The best combination of optimization method and dropout was determined in training time over a validation set, using the *4-fold cross validation* approach by 60 epochs and batchsize equal to 4, varying over the three optimization

| | Mean IoU | |
|-----------|-----------------|---------------|
| Optimizer | Dropout = 0.001 | Dropout = 0.5 |
| RMSprop | <u>0.44253</u> | 0.3117 |
| Adam | 0.240277 | 0.315714 |
| SGD | 0.000886 | 0.00151 |

Table 2: For each combination of optimizer and dropout values the simple mean is reported between 12 IoU corresponding to the 3 variants considered in each of the 4 folds.

methods and the two dropout values. The values selected were those that maximize the mean of Jaccard’s *Intersection-over-Union* (IoU) (Jaccard, 1912), a typical assessment measure in segmentation problems (see Section 3.1.2). For each combination of optimizer and dropout values the simple mean is reported between 12 IoU corresponding to the 3 variants considered in each of the 4 folds. It can be observed in Table ~2 that the combination of parameters with which the highest average IoU is reached is RMSProp with a dropout of 0.001.

Finally , the 3 variants were trained with RMSProp as an optimization method and a dropout value of 0.001 over the complete training set for 200 epochs and batch size equal to 4.

2.3.3. SW approach training

The training stage for this approach is conducted in the same way as for the original workflow proposed in Pérez et al. (2017). This involves training a binary classifier to learn the concept of bud versus non-bud from a collection of rectangular patches that may or may not contain a bud. During the training, bud patches must be regions that perfectly circumscribe the bud while non-bud patches must be regions that do not contain a single bud pixel (see Figure ~2). Therefore, to build the patch collection, the 558 images and their masks were processed following the same protocol as in Pérez et al. (2017), obtaining a total of 558 patches circumscribing each bud (one per image) and more than 25000 non-bud patches (the non-bud area is much larger than the area occupied by a bud in the image). The size of these patches is variable, with resolutions between 0.1 and 2.6 megapixels approximately (patches from 100×100 to 1600×1600 pixels).



Figure 2: Collection of patches used in this work. The first and second rows correspond to bud patches and non-bud patches, respectively. Image extracted from perez2017image.

From this collection of patches, a balanced patch train set was created, i.e., with 558 patches of each class, where non-bud patches were taken at random from thousands of patches. The training was performed as detailed in the pipeline proposed by Pérez et al. (2017): (i) all SIFT descriptors were extracted from the train set; (ii) BoF was applied with a vocabulary size equal to 25, since it was the model with the best results according to the authors; and (iii) the SVM classifier was trained on the BoF descriptors of each patch using a *Radial Basis Function* kernel, where the value of the γ and C parameters was established by means of a 5-fold cross-validation on the same value ranges, i.e., $\gamma = \{2^{-14}, 2^{-13}, \dots, 2^{-7}\}$ and $C = \{2^5, 2^6, \dots, 2^{14}\}$.

3. Experimental results

In this section, a systematic evaluation of the quality of our proposed FCN-MN procedure for bud detection quality is presented. According to the discussion in the introduction, it can be decomposed into the three aspects that affect the relevant bud-related variables listed in Table ~1: *segmentation*, *correspondence identification*, and *localization*.

For that purpose, the following subsection starts by presenting metrics that quantify the quality of these aspects, followed by the results in subsection ~3 that presents details on the metric values obtained for different experiments over the image test set.

414 3.1. Performance metrics

415 3.1.1. Correspondence identification metrics

416 Correspondence identification of buds, both in FCN-MN and SW, is the
417 result of two steps: (i) the thresholding of the algorithm’s output mask into
418 a *binary mask*, keeping all pixels of ν the probabilistic mask output by FCN-
419 MN with values higher than τ , and keeping all pixels that belong to at least
420 ν patches rendered positive by SW, and (ii) the association of each *connected*
421 *component* of the binary mask to exactly one (detected) bud.

422 Therefore, an incorrect correspondence identification is the result of an in-
423 correct matching of detected components with actual buds in the image. This
424 matching can become extremely complicated when there is an unknown number
425 of true buds in the scene, as can be seen by the large amount of possible detec-
426 tion metrics defined in [Oguz et al. \(2017\)](#). To simplify the analysis, our image
427 collection contains a single bud per image, avoiding the need for all the metrics
428 that report the confusing situation of a component overlapping more than one
429 true bud. This results in the following simplified list of possible metrics:

- 430 • **Correct Detection** (CD) is the best case and counts all images in the test
431 collection for which the detected binary mask presents a single connected
432 component, and this connected component overlaps with the true bud of
433 the image. This would correspond with a *true positive* situation.
- 434 • **Split** (S) occurs when there is more than one detection per bud, which
435 happens when the mask contains multiple connected components, all of
436 which overlaps the true bud. This metric counts the total number of
437 images of the test collection whose detection is split.
- 438 • **False Alarm** (FA) is equivalent to a *false positive* situation and cor-
439 responds to connected components not overlapping the true bud. This
440 measure counts the total number of such components over all images in
441 the test collection.
- 442 • **Detection Failure** (DF) is equivalent to a *false negative* situation when
443 the detection mask presents no connected components. It counts one for
444 each image that satisfies this condition.

445 All four cases are mutually exclusive, that is, no image can satisfy any two
 446 (or more) of these definitions simultaneously. To quantify the correspondence
 447 identification quality, one could simply report these quantities counted over the
 448 test set, with the best case consisting in a CD value equal to the cardinality of
 449 this set. However, determining the overall correspondence identification quality
 450 from the analysis of 4 quantities can become rather complicated.

451 One alternative is reporting the well-known precision and recall, denoted
 452 as P_D and R_D , and referred to as *detection-precision* and *detection-recall* to
 453 distinguish them from the segmentation precision and recall defined further
 454 down. For that, the fact that there are two different true positive counts, CD
 455 and S , needs to be addressed first. This is solved by first counting as true
 456 positives not only the CD type of images, but also S , i.e., any image with either
 457 a correct detection or a split case is counted as one true positive, resulting in:

$$P_D = \frac{\text{true positives}}{\text{true positives} + \text{false positives}} = \frac{CD + S}{CD + S + FA} \quad (1)$$

$$R_D = \frac{\text{true positives}}{\text{true positives} + \text{false negatives}} = \frac{CD + S}{CD + S + DF}, \quad (2)$$

458 and then account for the split type of errors by explicitly reporting S .

459 Given these quantities, the *F1-measure* computed as their harmonic average
 460 is also reported:

$$F1 = 2 \times \frac{\text{precision} \times \text{recall}}{\text{precision} + \text{recall}}.$$

461 3.1.2. Segmentation metrics

462 Correspondence identification metric, although informative, relies on the
 463 overlap between detected and true buds, regardless of how minimal the over-
 464 lap is. This could miss several possible pixel-wise detection errors, resulting
 465 in rather coarse comparisons between competing detection algorithms. For in-
 466 stance, a correct detection could present a very small overlap with the true bud,
 467 with many or even a majority of the true bud pixels missing (i.e., several *false*
 468 *negative* pixels), or it could be erroneously reporting several pixels as bud pixels
 469 (i.e., several *false positive* pixels). Clearly, the best case scenario would be a case
 470 of correct detection with no false negative or positive pixels that would visually

correspond to a perfect overlap between the detected connected component and the true bud.

Similarly, a pixel-wise comparison of the masks could help assess split quality. The best split, for instance, would be one completely enclosed within the true mask -i.e., with none of its connected components presenting false positive pixels-, while covering as much of the true bud mask as possible, i.e., presenting just enough false negatives to disconnect its components. Finally, a false alarm case, clearly presenting only false positive pixels, could be further assessed by the number of (false positive) pixels in its components.

The community has proposed several metrics to quantify segmentation errors. The most obvious ones are those that report the *fraction* of the whole image corresponding to *true positive* pixels, denoted as *TPF*; *false positive* pixels, denoted as *FPF*; and *false negative* pixels, denoted as *FNF*. As for the correspondence identification metric, one can simplify the analysis by considering pixel-wise precision and recall, denoted as P_S and R_S and referred to as *segmentation precision* and *segmentation recall*, defined formally as:

$$\begin{aligned} P_S &= TPF / (TPF + FPF) \\ R_S &= TPF / (TPF + FNF), \end{aligned}$$

accompanied by their weighted harmonic mean, the well-known *F-measure*,

$$2 \times \text{precision} \times \text{recall} / (\text{precision} + \text{recall}), \quad (3)$$

proposed independently by [Dice \(1945\)](#); thus, usually referred to as the *Dice measure*. A common alternative to the Dice measure is Jaccard's *intersection-over-union* ([Jaccard, 1912](#)) equivalent to $TPF / (TPF + FPF + FNF)$.

With these metrics, one could quantify the refinements discussed in the first paragraph above by simply applying them, not to the whole mask, but to the individual correspondence identification cases; for instance, by reporting the mean Dice measured over all correctly detected components. Or else, by refining the assessment of how bad a split is, one could report the mean Dice measure to all components of some split or the mean Dice measure over all split components of all split images.

498 The case of false alarms is rather monotonous and not very informative
 499 with zero precision and recall for all such components. Indeed, a pixel-wise
 500 assessment of the gravity of a false alarm requires a quantification of the number
 501 of false positive pixels. One could simply consider the *FPF*, the fraction of all
 502 the false positive image pixels. Instead, we considered a normalization against
 503 bud size to be more informative, resulting in the *normalized area*, denoted as
 504 *NA* and defined formally as *the total area of the component corresponding to its*
 505 *total number of pixels normalized by the area of the true bud*.

506 3.1.3. Localization metrics

507 As a localization metric we propose the *normalized distance*, denoted as *ND*,
 508 defined formally as *the distance between the center of mass of the component*
 509 *and the center of mass of the true bud, divided by the diameter of the true bud*
 510 *(defined as the maximum distance between any two border points of the true*
 511 *bud)*.

512 3.2. Results

513 We shall proceed now to assess the validity of our main hypothesis, namely,
 514 that FCN-MN is a better detector than its SW counterpart over each of the
 515 metrics defined in the previous section.

516 For a thorough comparison, several cases for each algorithm were considered:
 517 training 27 FCN-MN detectors and 40 SW detectors over the training set of 558
 518 images, one for each combination of their respective hyper-parameters. For
 519 FCN-MN, these hyper-parameters are the three architectures -8s, 16s, and 32s-
 520 and the 9 values $\{0.1, 0.2, \dots, 0.9\}$ for the binarization threshold τ . For SW,
 521 in turn, these hyper-parameters are the 10 patch sizes $\{100, 200, \dots, 1000\}$ and
 522 the 4 values $\{1, 2, 3, 4\}$ of the voting threshold ν .

523 Table ~3 shows the results for the best detectors of each algorithm, report-
 524 ing all performance metrics of the three aspects of detection: correspondence
 525 identification, segmentation and localization. The first column shows the la-
 526 bel of the selected detectors, with the subscript indicating the architecture and
 527 patch size for the case of FCN-MN and SW, respectively, and the superscript
 528 indicating the thresholds τ and ν , respectively.

529 The table includes all metrics defined in Section ~3.1 required for a thor-
530 ough comparison of FCN-MN against SW. First, four correspondence identifi-
531 cation metrics are included: detection precision P_D , detection recall R_D , the
532 F1-measure $F1$, and S (the total count of split components).

533 For a thorough analysis of the segmentations, the segmentation metrics for
534 the correct detections, splits and false alarms were differentiated. For the de-
535 tectations -i.e., correct detections and splits-, we report segmentation precision,
536 segmentation recall, and the Dice measure denoted in the table by P_S^{CD} , R_S^{CD}
537 and $Dice^{CD}$ for correct detections and P_S^S , R_S^S and $Dice^S$ for splits. Each of
538 the three correctly detected cells report the mean value of the measure com-
539 puted for each correctly detected test image, i.e., each image with only one
540 component overlapping the true bud, including the corresponding standard de-
541 viation in parenthesis. For the split group, the mean and standard deviation
542 are computed over the measures computed only for the split images, i.e., over
543 the images containing at least two components overlapping the true bud. Here,
544 the segmentation metrics are computed over the union of all split components.

545 For the false alarms, the mean *normalized area* (NA) is reported, in this case
546 computed individually for each false alarm component, reporting at each cell its
547 mean over all false alarm components of all test images. Finally, for localization,
548 the table reports the *normalized distance* (ND), but *only* the mean and standard
549 deviation (in parenthesis) over all false alarms components. As they overlap the
550 true bud, correctly detected and splitted components should be so close to the
551 true bud that no major analysis should be necessary. We thus report in column
552 ND the mean normalized distance of each false alarm connected component
553 that appears in any test image, and include within the analysis of the table
554 some results for the correct detections and splits that confirm the closeness to
555 the true bud. But for the sake of completeness, some statistics are included
556 below.

557 The table is a summary, as it includes only a subset of all 27 FCN-MN cases
558 and a subset of all 40 SW cases. A detector was considered for inclusion in the
559 table if, when compared to its counterparts of the same algorithm, it resulted
560 in the highest value for at least one of the metrics. The corresponding cell was
561 marked in bold in the table. For instance, the detector FCN-MN_{16s}^{0.8} has been

562 included because its detection precision P_D of 97.7% is the largest among the
563 detection precision of all 27 FCN-MN detectors. Similarly, the detector SW₁₀₀₀¹
564 has been included because its precision $P_D = 67.0\%$ is the largest among all 40
565 SW detectors.

566 The table shows a clear improvement of FCN-MN over SW. For all metrics,
567 the best FCN-MN detector (bolded) improves (or ties) over the best SW detec-
568 tor (bolded) represented in the table by underlying the detector with the best
569 metric. The exception is the two segmentation recalls (for correct detections
570 and splits) for which the SW case has a better (larger) mean, 98.8% versus
571 99.9% for correct detections and 74.7% versus 78.6% for the split case; and the
572 total split count S , with the best case for FCN-MN being 1 and 0 for the best
573 SW case. These improvements are not statistically significant, however, due to
574 the large standard deviations of the FCN-MN cases, of 3.4 and 8.1 for correct
575 detections and splits, respectively, resulting in (statistically) overlapping values.

576 In some cases, the improvements of FCN-MN over SW are overwhelming. For
577 instance, for detection-precision, correctly detected segmentation-precision, and
578 split segmentation-precision, the FCN-MN over SW improvements are 97.7%
579 versus 67.0%, 98.1% versus 46.5%, and 99.9% versus 67.5%, respectively. In
580 addition, for the NA and ND of false alarms, the FCN-MN versus SW im-
581 provements are 0.04 versus 0.22 and 1.1 versus 6.0, respectively. As mentioned,
582 we omitted in the table the mean normalized distances for correct detections
583 and splits, but for completeness let us present their minimum and maximum
584 values. For each FCN-MN and SW detector we computed the resulting mean
585 normalized distance over all correctly detected components in the test set, on
586 one hand, and over all split components in the test set on the other. Among
587 all FCN-MN detectors, the *minimum* and *maximum* mean (and standard de-
588 viation in parentheses) normalized distance of correctly detected components
589 are $ND = 0.049(0.055)$ and $ND = 0.081(0.145)$, respectively. Similarly, the
590 minimal and maximal pair for the splitted components mean (and standard
591 deviation) normalized distance is $ND = 0.261(0.179)$ and $ND = 0.429(0.066)$,
592 respectively. As predicted, all rather small, with both the minimum and max-
593 imum mean distance falls within one diameter of a true bud. When compared
594 to the SW detectors, the min/max pair of mean normalized distances for the

correctly detected components is $ND = 0.383(0.2089)/ND = 1.352(1.43)$, and
for for splits components is $ND = 0.329(0.206)/ND = 1.152(0.023)$, respec-
tively. As can be observed, again FCN-MN shows an improvement over SW,
with no statistically significant overlap of their min/max interval for the correct
detections, and a minor statistically significant overlap for the splits (where the
maximum value $0.429 + 0.066$ for FCN-MN, is overlapping the minimum value
 $0.329 - 0.206$ of SW.

3.2.1. Detailed analysis of correspondence identification metrics

Graphically, one could expect a better combined analysis of detection-precision
and detection-recall than could be obtained by comparing the F1-measure. This
is shown as a scatter plot in Figure ~3, a graphical representation of a non-
summarized version of the second and third columns of Table ~3. Each dot
in the plot is located according to the detection-precision and detection-recall,
and the color black or white, whether it corresponds to an FCN-MN or an SW
detection model.

The graph reinforces the clear and undisputed improvements of FCN-MN
over SW already detected in the table, with similar detection-recalls, but larger
detection-precisions over most scenarios.

Detection-precision and detection-recall are computed over a combination of
correctly detected and splitted components. To easily assess the impact of the
split cases, Figure ~4 shows the S values corresponding to the fifth column of
a (non-summarized version of) Table ~3 in the form of a histogram, with bins
representing values of S and the bars for that bin representing the proportion of
models that resulted in that value of S . Black and white bars discriminate the
cases for FCN-MN and SW, respectively. For instance, the first bin indicates
that approximately 54% of the FCN-MN models and approximately 62% of the
SW models resulted in a total number splits of less than 5. Overall, the FCN-MN
distribution is slightly more concentrated in the lower number of splits than the
SW distribution, but in general both algorithms compare fairly, with no clear
contender when compared with the average number of splits they produce.

| Detector | P_D | R_D | $F1$ | S | P_S^{CD} | R_S^{CD} | $Dice^{CD}$ | P_S^S | R_S^S | $Dice^S$ | NA | ND |
|--------------------------------------|-------------|------------|-------------|----------|--------------------|-------------------|--------------------|--------------------|--------------------|--------------------|--------------------|-------------------|
| FCN-MN ^{0.5} _{8s} | 75.4 | 98.6 | 85.4 | 2 | 91.0 (11.3) | 90.2 (11.7) | 89.6 (10.3) | 96.6 (2.2) | 73.1 (17.6) | 82.1 (10.2) | 0.26 (0.69) | 3.72 (4.64) |
| FCN-MN ^{0.9} _{8s} | 90.1 | 97.1 | 93.5 | 8 | 98.1 (6.0) | 68.3 (21.1) | 77.9 (19.6) | 98.7 (3.0) | 57.4 (18.4) | 70.8 (13.6) | 0.24 (0.5) | 3.8 (5.66) |
| FCN-MN ^{0.1} _{16s} | 71.3 | 100 | 83.2 | 6 | 75.7 (13.1) | 95.4 (14.7) | 83.1 (13.5) | 83.1 (8.9) | 54.1 (21.9) | 61.9 (17.5) | 0.12 (0.44) | 5.27 (6.53) |
| FCN-MN ^{0.4} _{16s} | 87.0 | 96.4 | 91.5 | 1 | 87.7 (12.1) | 89.8 (18.2) | 87.0 (15.6) | 96.7 (0.0) | 37.0 (0.0) | 53.5 (0.0) | 0.04 (0.09) | 3.8 (5.08) |
| FCN-MN ^{0.6} _{16s} | 95.6 | 93.6 | 94.6 | 3 | 92.2 (8.7) | 88.2 (13.3) | 89.1 (10.7) | 99.4 (0.6) | 16.2 (10.6) | 26.6 (16.8) | 0.08 (0.11) | 1.1 (0.65) |
| FCN-MN ^{0.8} _{16s} | 97.7 | 92.1 | 94.9 | 4 | 95.8 (7.0) | 81.6 (14.6) | 87.0 (10.7) | 99.7 (0.3) | 34.2 (32.6) | 43.9 (33.1) | 0.1 (0.12) | 1.28 (0.95) |
| FCN-MN ^{0.9} _{16s} | 97.7 | 91.4 | 94.5 | 4 | 97.6 (5.6) | 74.5 (16.5) | 83.1 (12.8) | 99.9 (0.1) | 31.8 (27.9) | 41.6 (34.0) | 0.07 (0.11) | 1.33 (0.9) |
| FCN-MN ^{0.1} _{32s} | 35.4 | 100 | 52.2 | 8 | 67.4 (14.0) | 98.8 (3.4) | 79.1 (11.0) | 86.0 (9.4) | 73.4 (19.6) | 77.1 (10.4) | 0.14 (0.66) | 4.62 (5.59) |
| FCN-MN ^{0.2} _{32s} | 50.9 | 100 | 67.5 | 10 | 73.9 (13.6) | 98.1 (3.8) | 83.5 (10.1) | 92.2 (5.4) | 53.4 (25.8) | 63.6 (19.3) | 0.17 (0.55) | 4.33 (6.17) |
| FCN-MN ^{0.3} _{32s} | 49.8 | 100 | 66.5 | 10 | 79.1 (13.2) | 95.5 (10.5) | 85.2 (11.8) | 88.5 (9.7) | 61.0 (35.1) | 65.8 (28.2) | 0.1 (0.39) | 3.68 (5.62) |
| FCN-MN ^{0.6} _{32s} | 68.5 | 99.3 | 81.1 | 16 | 89.0 (11.5) | 89.1 (11.3) | 88.1 (9.6) | 92.4 (7.7) | 74.7 (28.1) | 78.1 (24.0) | 0.11 (0.3) | 2.95 (4.36) |
| SW ¹ ₁₀₀ | 9.4 | 100 | 17.2 | 28 | 24.6 (17.7) | 86.7 (19.5) | 33.6 (15.1) | 57.9 (28.2) | 24.8 (16.8) | 27.9 (13.8) | 1.08 (3.2) | 7.68 (6.02) |
| SW ³ ₁₀₀ | 14.6 | 93.1 | 25.3 | 40 | 42.4 (26.4) | 56.8 (29.9) | 39.9 (19.7) | 55.5 (32.2) | 24.8 (18.1) | 26.0 (15.6) | 0.31 (0.96) | 6.45 (6.19) |
| SW ⁴ ₁₀₀ | 19.5 | 87.4 | 31.9 | 49 | 46.5 (29.3) | 39.2 (28.9) | 33.9 (21.1) | 49.0 (29.0) | 20.1 (13.7) | 24.1 (14.0) | 0.22 (0.57) | 6.0 (6.56) |
| SW ¹ ₂₀₀ | 20.0 | 100 | 33.3 | 12 | 16.6 (12.5) | 94.9 (13.5) | 25.9 (14.2) | 49.3 (26.4) | 40.2 (17.4) | 36.8 (11.9) | 5.13 (19.3) | 7.56 (5.35) |
| SW ³ ₂₀₀ | 26.0 | 98.6 | 41.1 | 19 | 29.9 (17.0) | 74.7 (27.3) | 38.5 (17.0) | 67.5 (32.7) | 16.5 (8.9) | 24.2 (11.9) | 1.69 (3.15) | 8.94 (6.22) |
| SW ³ ₃₀₀ | 26.9 | 100 | 42.4 | 2 | 13.7 (13.6) | 97.0 (9.6) | 21.6 (15.5) | 55.0 (11.8) | 48.1 (1.1) | 50.8 (4.5) | 7.79 (20.5) | 6.83 (4.44) |
| SW ⁴ ₄₀₀ | 32.7 | 100 | 49.3 | 2 | 10.5 (11.7) | 98.7 (9.3) | 17.2 (15.3) | 42.6 (10.1) | 61.9 (11.6) | 50.4 (10.9) | 11.59 (24.05) | 7.12 (4.15) |
| SW ² ₄₀₀ | 34.6 | 100 | 51.4 | 4 | 15.6 (15.1) | 94.5 (13.3) | 23.8 (15.6) | 48.7 (27.6) | 36.0 (4.6) | 38.6 (13.1) | 9.54 (26.13) | 7.88 (4.89) |
| SW ¹ ₅₀₀ | 40.2 | 100 | 57.3 | 1 | 8.40 (9.7) | 99.9 (4.9) | 14.2 (13.8) | 17.9 (0.0) | 78.6 (0.0) | 29.2 (0.0) | 17.39 (30.07) | 7.22 (4.04) |
| SW ² ₅₀₀ | 38.6 | 100 | 55.7 | 1 | 13.5 (14.0) | 95.2 (14.5) | 21.0 (16.0) | 35.2 (0.0) | 45.9 (0.0) | 39.8 (0.0) | 17.19 (39.07) | 7.56 (4.42) |
| SW ¹ ₆₀₀ | 43.5 | 100 | 60.6 | 0 | 6.9 (7.8) | 98.5 (10.7) | 12.0 (12.0) | nan (nan) | nan (nan) | nan (nan) | 25.48 (48.45) | 7.72 (4.3) |
| SW ² ₆₀₀ | 41.7 | 100 | 58.8 | 1 | 10.4 (10.6) | 93.7 (18.9) | 17.2 (14.4) | 19.7 (0.0) | 27.2 (0.0) | 22.9 (0.0) | 20.41 (38.32) | 7.92 (4.38) |
| SW ¹ ₇₀₀ | 50.6 | 100 | 67.2 | 0 | 5.6 (6.5) | 98.6 (12.0) | 9.9 (10.3) | nan (nan) | nan (nan) | nan (nan) | 31.95 (64.36) | 7.75 (4.45) |
| SW ¹ ₈₀₀ | 56.7 | 100 | 72.4 | 0 | 5.1 (6.6) | 97.7 (11.0) | 9.0 (10.4) | nan (nan) | nan (nan) | nan (nan) | 44.53 (71.52) | 7.7 (4.06) |
| SW ² ₈₀₀ | 49.6 | 99.2 | 66.1 | 0 | 8.3 (9.4) | 95.0 (15.9) | 13.9 (13.2) | nan (nan) | nan (nan) | nan (nan) | 30.52 (46.45) | 7.82 (4.1) |
| SW ¹ ₉₀₀ | 64.3 | 100 | 78.3 | 0 | 4.2 (5.7) | 94.7 (19.0) | 7.5 (9.2) | nan (nan) | nan (nan) | nan (nan) | 48.16 (80.31) | 7.9 (4.35) |
| SW ³ ₉₀₀ | 42.2 | 92.4 | 58.0 | 0 | 15.0 (14.8) | 81.5 (28.9) | 22.7 (16.8) | nan (nan) | nan (nan) | nan (nan) | 17.97 (29.56) | 7.65 (4.67) |
| SW ¹ ₁₀₀₀ | 67.0 | 100 | 80.2 | 0 | 3.7 (4.7) | 95.3 (18.3) | 6.8 (7.9) | nan (nan) | nan (nan) | nan (nan) | 57.83 (84.87) | 7.91 (4.3) |
| SW ² ₁₀₀₀ | 56.7 | 98.3 | 71.9 | 0 | 6.3 (6.9) | 93.8 (19.1) | 11.1 (10.9) | nan (nan) | nan (nan) | nan (nan) | 47.26 (68.92) | 7.98 (4.44) |

Table 3: Correspondence identification, segmentation and localization metrics for the best FCN-MN and SW detection models. Each column shows two bolded cells corresponding to the cell with the best metric among all FCN-MN rows and the cell with best metric among SW rows. The larger of the two has been underlined, representing the best among all combined models, i.e., the best of the column. Columns P_D , R_D , $F1$ and S show results for the *Correspondence identification metrics* detection precision, detection recall, F1-measure and number of images with splits, respectively; Columns P_S^{CD} , R_S^{CD} and $Dice^{CD}$ (resp. P_S^S , R_S^S and $Dice^S$) correspond to the *segmentation metrics* mean segmentation precision, mean segmentation recall, and mean Dice measure over all correctly detected components (resp. split components); and Columns NA and ND show the mean NA and mean ND over all false alarm components.

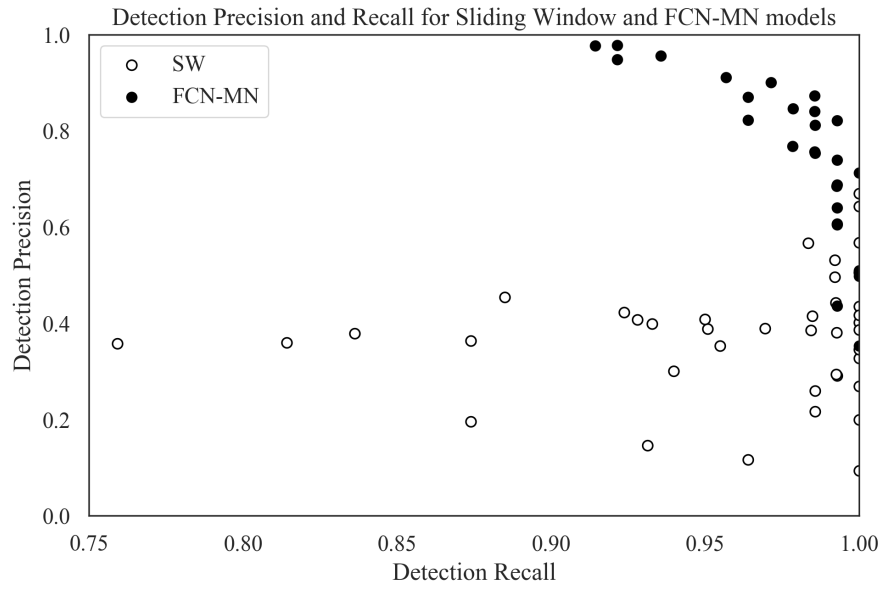


Figure 3: Precision-Recall scatterplots of the second and third columns of Table ~3 discriminating the results for FCN-MN and SW with black and white dots, respectively. Each dot then represents the detection-precision and detection-recall computed over all test images, for some particular configurations of hyper-parameters. For FCN-MN, these hyper-parameters would be the architecture, with values 8s, 16s and 32s, and threshold $\tau = \{0.1, 0.2, \dots, 0.9\}$ for a total of 27 black dots, while for SW, the hyper-parameters would be the patch sizes $\{100, 200, \dots, 1000\}$ and voting thresholds $\{1, 2, 3, 4\}$ for a total of 40 white dots.

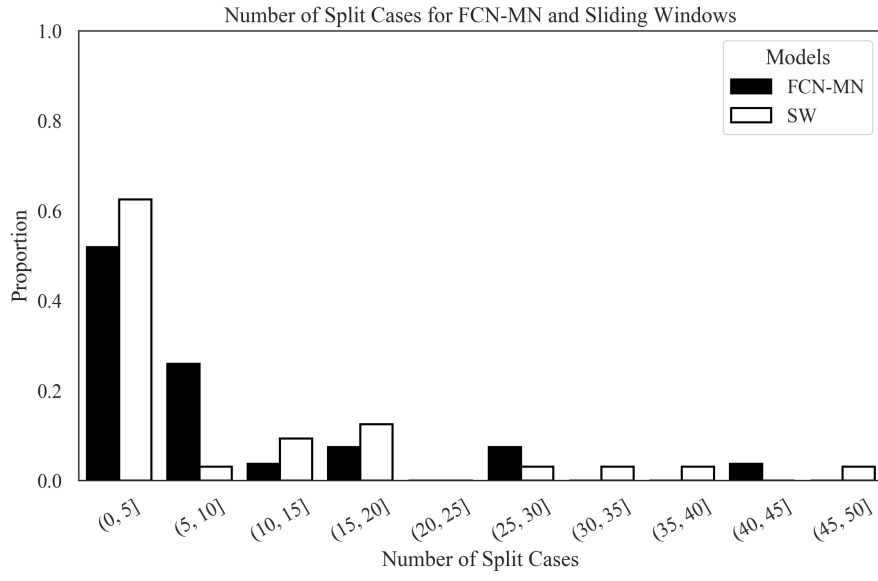


Figure 4: Histogram reporting the distribution of S for FCN-MN and SW in black and white bars, respectively. Each bar represents the proportion among all models (27 for FCN-MN and 40 for SW) that contains the number of splits indicated by the bin label. For instance, the first (from left to right) white bar indicates that almost 14% out of the 40 SW models contains between 0 and 5 splits.

3.2.2. Detailed analysis of segmentation metrics

As for the correspondence identification metric, Figures~ 5a and 5b show scatter plots for segmentation-precision and segmentation-recall and for *correct detection* and *split* cases, respectively. These correspond to their respective columns of (a non-summarized version of) Table ~3 with black and white dots representing the values of FCN-MN and SW detection models, respectively. The position of each dot in the plot corresponds to the mean segmentation-precision and mean segmentation-recall over all images in the test set, computed over the correctly detected components (splitted components, respectively) of the masks produced by the detection model associated to that dot. The standard deviation of the recall (precision) is shown as a horizontal (vertical) bar.

In Figure ~5a (correct detections), one can observe that all black dots (FCN-MN) are clustered in the upper-right corner of the graph, enclosed by a minimum precision of approximately 65% and minimum recall of approximately 60%, while the white dots (SW) are clustered in the lower-right corner of the graph with maximum precisions of 50% and recall ranging from approximately 35% to 100%. Overall, both algorithms show relatively high recalls, but with FCN-MN reaching much larger precisions. We can point to the coarse detection of the SW method as the main cause for low precision, as this is reduced when extra, false positives are present in the positive mask.

In Figure ~5b (splits), one can observe again the overwhelming improvements of FCN-MN over SW, with all (but one) SW cases presenting precisions under 60%, with the outlier showing a precision of nearly 70% and a similar distribution of recall values.

The segmentation results for the false alarm, the *NA* for each of the 27 models of FCN-MN and each of the 40 models of SW, i.e., for each cell in the one-before-last column of (a non-summarized version of) Table ~3 are reported graphically. Figure ~6 shows these results grouped in the form of two histograms, one for the FCN-MN detection models (black) and one for the SW models (white). Bars in the histogram represent the proportion of detection models whose mean *NA* (over all false alarm components of all images) falls within the bin interval. The more concentrated to the left the better the algorithm, as this indicates that more detection models for that algorithm resulted

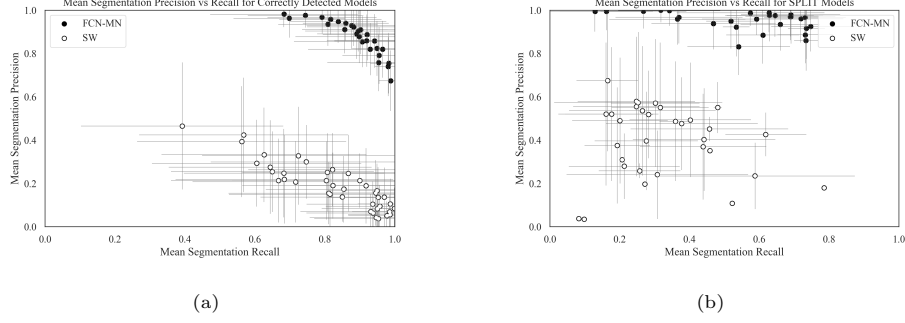


Figure 5: Segmentation Precision-Recall scatterplots reporting the results for FCN-MN and SW in black and white, respectively, with dots representing the segmentation precision and segmentation recall average over all images in the test set (and bars representing standard deviations) with one dot per hyper-parameter configuration (27 for FCN-MN and 40 for SW). In (a) averages were computed over the segmentation precision and recall of correctly detected components, while in (b), averages were computed over the segmentation precision and recall of split components. Standard deviations.

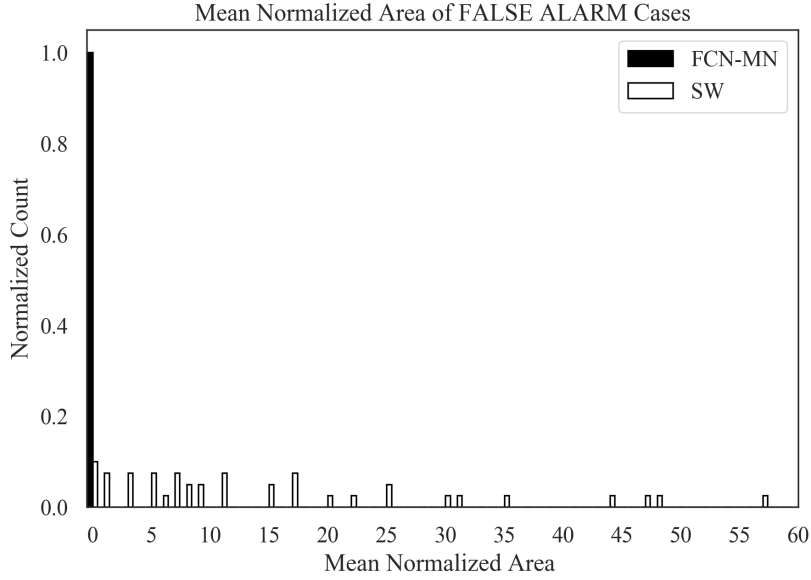


Figure 6: FCN-MN (black bars) and SW (white bars) histograms of the mean normalized area NA of false alarm components with bars representing the proportion of detection models whose mean NA falls within the bin interval.

658 in smaller NA (on average).

659 One can observe the histogram for FCN-MN considerably more concentrated
660 in the left-most part of the histogram than that of SW, with all FCN-MN
661 concentrated in a single bar at the left-most interval of $[0.0, 1.0)$. For SW,
662 the situation is rather different with bars at intervals as far to the right as
663 $[57.0, 58.0)$, that is, detection models with areas as large as 58 times the bud
664 area.

665 3.2.3. Detailed analysis of localization metrics

666 To conclude, this subsection presents a graphical representation of the lo-
667 calization results reported in Table ~3, that is, the *normalized distance* (ND)
668 only for false alarms. This assumes that, because they overlap the true bud,
669 correctly detected and split cases should be close enough to the true bud to
670 render unnecessary any analysis on their distance. Instead, a false alarm can be
671 arbitrarily far from the true bud.

672 Figure ~7 summarizes the ND values reported in the corresponding column
673 of the (non-summarized version) of Table ~3 in the form of two histograms, one
674 for FCN-MN (black) and one for SW (white). Bars in the histogram represent
675 the proportion of detection models (27 for FCN-MN and 40 for SW) whose
676 mean ND (over all false alarm components of all images) falls within the bin
677 interval. The more concentrated to the left the better the algorithm, as this
678 indicates that more detection models for that algorithm resulted in smaller ND
679 (on average).

680 Here again the advantage of FCN-MN over SW is clear, with the histogram
681 for FCN-MN more concentrated in the left-most part than that of SW, with
682 the FCN-MN histogram running from the $(0, 1]$ to the $(7, 8]$ bin and the SW
683 histogram running from the $(5, 6]$ towards the $(9, 10]$ bin.

684 4. Discussion and Conclusions

685 This section discusses the results obtained by the proposed approach in the
686 context of the problem of grapevine bud detection and its impact as a tool for
687 measuring viticultural variables of interest. It also highlights the most important
688 conclusions and presents future work.

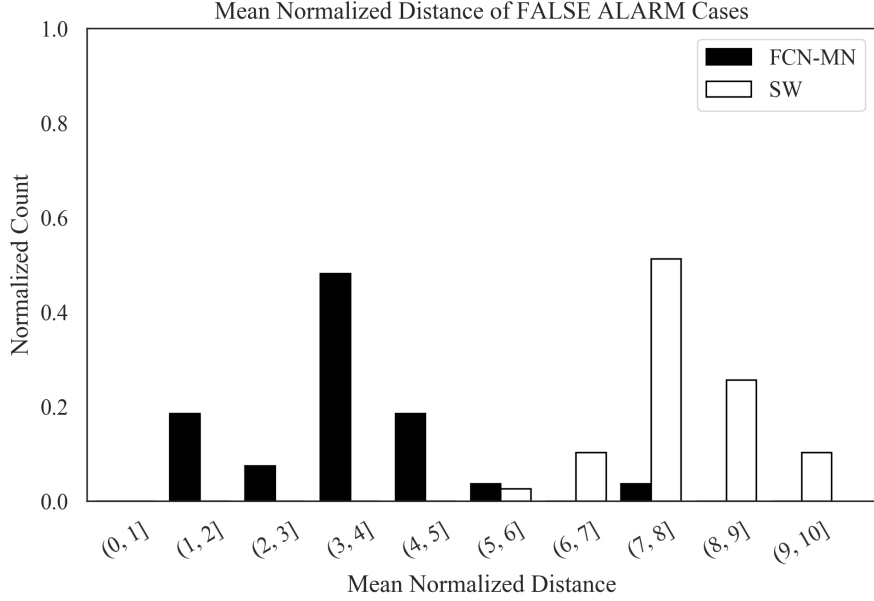


Figure 7: FCN-MN (black bars) and SW (white bars) histograms of mean normalized distance ND over all false alarm components with bars representing the proportion of detection models whose mean ND falls within the bin interval.

689 This work introduces FCN-MN, a fully convolutional network with Mobile
690 Net architecture for the detection of grapevine buds in 2D images captured in
691 natural field conditions in winter (i.e., no leaves or bunches) and containing a
692 maximum of one bud.

693 The experimental results confirmed our main hypothesis: that the detection
694 quality achieved by FCN-MN is improved over the *sliding windows* detector
695 (SW) in all three detection aspects: segmentation, correspondence identification
696 and localization. Being SW the best bud detector known to these authors, one
697 can conclude that FCN-MN is a strong contender in the state-of-the-art for
698 bud detectors. However, even improving over these, one can still wonder if it
699 can address the main *quality* requirements of a practical measurement of the
700 bud-related variables in Table ~1.

701 Quality performance could be assessed by the metrics reported in Table ~3.
702 In the best case, FCN-MN shows a detection-precision and detection-recall of
703 97.7% and 100%, respectively, a mean (and standard deviation) segmentation-
704 precision and segmentation-recall for correct detections of 98.1%(0.6) and 98.8%(3.4),

705 respectively, and for splits 99.9%(0.1) and 74.7%(28.1), respectively. For false
706 alarms, it shows a maximum NA of 0.04(0.09) and a maximum ND of 0.04(0.22).

707 However, each of these maximums correspond to different FCN-MN detec-
708 tors. A better assessment must be conducted for a single detector. For that,
709 we picked FCN-MN_{16s}^{0.6} to show balanced quality overall. This detector reaches
710 detection precision and recall of 95.6% and 93.6%, respectively, meaning than
711 only 4.4% of all the detected connected components over all test images are false
712 alarms, and that only 6.4% of all true buds could not be detected (i.e., resulted
713 in detection failure).

714 Additionally, $S = 3$, meaning only 3 of all detections were splitted, which has
715 a segmentation precision of 99.4%(0.6) and a segmentation recall of 16.2%(10.6)
716 on average. The recall is rather small, suggesting that the split is, in fact, the
717 result of pixel-wise detection of the bud so sparse that it became disconnected.
718 In contrast, all remaining detections were correct (i.e., not splitted), reaching
719 segmentation precisions of 92.2%(8.7), a rather similar value to that of splits, but
720 a much larger mean segmentation recall of 88.2%(13.3). Overall, this resulted in
721 a mean Dice measure for the correct detections of 89.1%(10.7), demonstrating
722 a considerable (mean) coverage of the true bud with only 11.8% of the bud
723 pixels missing (on average) and only 7.8% of the detected pixels covering the
724 background (on average).

725 More promising, however, are the false alarm results with $NA = 0.08$ and
726 $ND = 1.1$, showing that these components are rather small covering only an
727 area that is 8% in size of the total bud area (on average) and distant to the true
728 bud by only 1.1(0.65) diameters.

729 Based on these results, what quality should one expect when the FCN-MN_{16s}^{0.6}
730 detector takes part in the measurement of the bud-related variables? For brevity,
731 this point is discussed for three variables from Table ~1: *bud number*, *bud area*,
732 and *internode length*.

733 The case of *bud number*, for example, requires identifying correspondences for
734 buds in the scene, so its quality will be impacted only by the metrics of detection
735 precision and recall (95.6% and 93.6%, respectively). To evaluate this impact,
736 we assume that a plant has approximately 240 buds on average. The number
737 of buds per plant depends on many factors, such as training system, grape

738 variety, type of treatment, time of year, among others, so this value is defined
739 as indicative to achieve an approximate analysis. For this case, a detection
740 precision of 95.6% would result in 11 buds counted in excess per plant, while a
741 recall of 93.6% would result in the omission of 15 buds in the count.

742 In addition, this model produces 3 splits with two components each, i.e. a
743 counting error in excess of 3% over the 140 buds in the test set. Particularly in
744 this analysis, it means that 6 new buds would be counted in excess, giving a total
745 of 17 buds in excess, practically cancelling out with the error of omission. But
746 additionally, these errors could in practice be statistically characterized allowing
747 for measurement correction towards more accurate values. Despite these good
748 results, our approach still has practical limitations for the measurement of bud
749 number due to the impossibility of automatically associating counts of the same
750 bud in two different images, making it difficult to massively measure the bud
751 count of a plant or plot.

752 The second variable of interest considered is *bud area*, where, in addition to
753 identifying correspondences for the buds of a scene, it is necessary to segment it
754 to estimate its area in pixels. Correspondence identification analysis is analogous
755 to bud counting, so now only segmentation metrics are discussed. From the
756 analysis developed in the previous paragraphs, it can be concluded that the
757 segmentation errors by splits and false alarms have a low impact in the general
758 results and, therefore, in the estimation of *bud area*. On the other hand, if we
759 compensate the segmentation errors for the correct detections (i.e. 11.8% of the
760 bud pixels missing and 7.8% of the detected pixels covering the background),
761 the area estimation error is only 4%. For illustrative purposes, we see that this
762 error is smaller than the precision error resulting from measuring the area of a
763 bud with a caliper. If we assume that the shape of a bud fits a circle, and that
764 the typical diameter of a bud is 5 mm, the resulting area is $19.63mm^2$. Since a
765 caliper has an accuracy of $0.1mm$, the area precision error would be $\pm 1.7mm^2$,
766 equivalent to 8.6% of the total area, a figure that doubles the 4% error produced
767 by our FCN-MN detector. To this difference, the error of manual measurement
768 resulting from assuming a circular bud shape must be added, an unnecessary
769 approximation in the case of FCN-MN.

770 As in the case of counting, these good results in measurement precision are

771 limited to achieve a practical use of this type of measurement because it is
772 impossible to automatically associate area measurements of the same bud in
773 two different images, making it difficult to systematically measure this variable
774 for the buds of a plant or plot. Furthermore, in this case, the areas obtained
775 are in pixels, which need to be converted into length or area magnitudes.

776 Finally, let us consider the case of *internode length*, estimated by the dis-
777 tance between buds of the same branch (by the closeness between buds and
778 nodes), which involves the operations of correspondence identification and lo-
779 calization. Again, correspondence identification analysis is analogous to bud
780 counting, which in this case will result in the reporting of more than one dis-
781 tance due to the detection of more than one component per bud. Among these
782 distances, we understand that the worst case can occur between false alarms
783 -these being the farthest from the true bud- and between two buds when the
784 false alarms are at a distance of ND from the farthest side of the other bud. On
785 average, it is $ND = 1.1$, which according to the typical diameter of vine buds is
786 equivalent to about 5mm, a value much lower than the typical bud distances of
787 approximately 15cm, i.e., about a 6.6% error in estimating the distance between
788 buds/nodes.

789 A limitation of our approach to achieving practical use of this type of mea-
790 surement is the possibility of determining when two buds are on the same branch,
791 which requires knowledge of the plant structure. Furthermore, with our method,
792 only the distance projected in the image plane could be measured, which can
793 arbitrarily differ from the actual distance in 3D. The greatest impact errors oc-
794 cur because of the excess or omission of connected components, with the excess
795 error exacerbated by the fact of associating detected buds with individual con-
796 nected components. A possible improvement to mitigate these errors would be
797 to apply some post-processing.

798 One such post-processing is *spatial clustering* of connected components group-
799 ing them by proximity. One could expect this to improve the results based on
800 the small areas of split and false alarm components. First, due to the closeness
801 of the false alarms to the true bud (small ND) -as well as the splits and cor-
802 rectly detected components (overlapping with it)-, and the fact that true buds
803 in real plants are typically tens or even hundreds of bud diameters apart, a sim-

804 ple spatial clustering of the components would connect all of them together as a
805 single, and correct, bud detection. Second, due to their small area -if clustered
806 together- the false alarm components would only slightly reduce segmentation
807 precision.

808 Another possible post-processing would be to rule out small connected com-
809 ponents, for example, whose area in pixels normalized to the total detected area
810 (sum of the areas of all connected components) is less than a certain threshold.
811 Improvements could be expected with this post-processing, since the results in
812 this work show that false alarms present small areas in relation to the true bud.
813 Lastly, connected component filters could be considered based on plant struc-
814 ture, for example, ruling out connected components that are far away from (or
815 do not overlap with) branches.

816 One could also consider in future works some improvements to overcome the
817 limitations for practical use mentioned above: (i) no associations between plant
818 parts of different images, (ii) distance and area measurements in pixels, (iii)
819 only 2D geometry, (iv) lack of knowledge of underlying plant structure, and (v)
820 need of images with no leaves.

821 One could also extend to buds the work of [Santos et al. \(2020\)](#) that addresses
822 limitation (i) for grape bunches. Limitation (ii) could be easily addressed by
823 adding to the visual scene some marker with known dimensions. This, how-
824 ever, requires such a marker in every image captured, a problem that could be
825 overcome by first producing a calibrated 3D reconstruction of the scene, i.e., a
826 3D reconstruction calibrated with a single marker in one of its frames ([Hartley
827 and Zisserman, 2003](#); [Moons et al., 2009](#)). In this way, every 2D image could
828 be calibrated against the 3D model, omitting the need for a marker. In addi-
829 tion, a 3D reconstruction of the scene could address limitation (iii) by locating
830 the detected buds in 3D space, following, for instance, the approach taken by
831 [Díaz et al. \(2018\)](#). Finally, a solution to limitations (iv) and (v) would require
832 an integrated approach involving the detection in 3D of branches and leaves,
833 respectively.

834 Acknowledgments

835 This work was funded by the National Technological University (UTN), the
836 National Council of Scientific and Technical Research (CONICET), Argentina,
837 and the National Fund for Scientific and Technological Promotion (FONCyT),
838 Argentina.

839 References

- 840 Berenstein, R., Shahar, O.B., Shapiro, A., Edan, Y., 2010. Grape clusters
841 and foliage detection algorithms for autonomous selective vineyard sprayer.
842 Intelligent Service Robotics 3, 233–243.
- 843 Bramley, R.G., 2009. Lessons from nearly 20 years of precision agriculture
844 research, development, and adoption as a guide to its appropriate application.
845 Crop and Pasture Science 60, 197–217.
- 846 Chum, O., Zisserman, A., 2007. An exemplar model for learning object classes,
847 in: 2007 IEEE Conference on Computer Vision and Pattern Recognition,
848 IEEE. pp. 1–8.
- 849 Collins, C., Wang, X., Lesefko, S., De Bei, R., Fuentes, S., 2020. Effects of
850 canopy management practices on grapevine bud fruitfulness. OENO One 54,
851 313–325.
- 852 Csurka, G., Dance, C., Fan, L., Willamowski, J., Bray, C., 2004. Visual cat-
853 egorization with bags of keypoints, in: Workshop on statistical learning in
854 computer vision, ECCV, Prague. pp. 1–2.
- 855 Dalal, N., Triggs, B., 2005. Histograms of oriented gradients for human detec-
856 tion, in: 2005 IEEE Computer Society Conference on Computer Vision and
857 Pattern Recognition (CVPR’05), pp. 886–893 vol. 1.
- 858 Diago, M.P., Correa, C., Millán, B., Barreiro, P., Valero, C., Tardaguila, J.,
859 2012. Grapevine yield and leaf area estimation using supervised classification
860 methodology on rgb images taken under field conditions. Sensors 12, 16988–
861 17006.

862 Díaz, C.A., Pérez, D.S., Miatello, H., Bromberg, F., 2018. Grapevine buds
863 detection and localization in 3d space based on structure from motion and 2d
864 image classification. *Computers in Industry* 99, 303–312.

865 Dice, L.R., 1945. Measures of the amount of ecologic association between species.
866 *Ecology* 26, 297–302.

867 Divvala, S.K., Hoiem, D., Hays, J.H., Efros, A.A., Hebert, M., 2009. An em-
868 pirical study of context in object detection, in: 2009 IEEE Conference on
869 computer vision and Pattern Recognition, IEEE. pp. 1271–1278.

870 Ferrari, V., Fevrier, L., Jurie, F., Schmid, C., 2007. Groups of adjacent contour
871 segments for object detection. *IEEE transactions on pattern analysis and*
872 *machine intelligence* 30, 36–51.

873 Garcia-Garcia, A., Orts-Escolano, S., Oprea, S., Villena-Martinez, V., Martinez-
874 Gonzalez, P., Garcia-Rodriguez, J., 2018. A survey on deep learning tech-
875 niques for image and video semantic segmentation. *Applied Soft Computing*
876 70, 41–65.

877 Grimm, J., Herzog, K., Rist, F., Kicherer, A., Töpfer, R., Steinhage, V., 2019.
878 An adaptable approach to automated visual detection of plant organs with
879 applications in grapevine breeding. *Biosystems Engineering* 183, 170–183.

880 Han, D., 2013. Comparison of commonly used image interpolation methods,
881 in: *Proceedings of the 2nd international conference on computer science and*
882 *electronics engineering*, Atlantis Press.

883 Hartley, R., Zisserman, A., 2003. *Multiple view geometry in computer vision*.
884 Cambridge university press.

885 Herzog, K., Kicherer, A., Töpfer, R., 2014a. Objective phenotyping the time of
886 bud burst by analyzing grapevine field images, in: *XI International Confer-*
887 *ence on Grapevine Breeding and Genetics* 1082, pp. 379–385.

888 Herzog, K., et al., 2014b. Initial steps for high-throughput phenotyping in
889 vineyards. *Australian and New Zealand Grapegrower and Winemaker* , 54.

- Hirano, Y., Garcia, C., Sukthankar, R., Hoogs, A., 2006. Industry and object recognition: Applications, applied research and challenges, in: Toward category-level object recognition. Springer, pp. 49–64.
- Howard, A.G., Zhu, M., Chen, B., Kalenichenko, D., Wang, W., Weyand, T., Andreetto, M., Adam, H., 2017. Mobilenets: Efficient convolutional neural networks for mobile vision applications. arXiv preprint arXiv:1704.04861 .
- Institute, T.A.W.R., a. Viticare on Farm Trials - Manual 3.1: Measuring Fruit Quality. 1 ed. The Australian Wine Research Institute. Accessed August 2020.
- Institute, T.A.W.R., b. Viticare on Farm Trials - Manual 3.3: Vine Health. 1 ed. The Australian Wine Research Institute. Accessed August 2020.
- Jaccard, P., 1912. The distribution of the flora in the alpine zone. 1. New phytologist 11, 37–50.
- Kahng, M., Andrews, P.Y., Kalro, A., Chau, D.H.P., 2017. A ctiv is: Visual exploration of industry-scale deep neural network models. IEEE transactions on visualization and computer graphics 24, 88–97.
- Kaymak, Ç., Uçar, A., 2019. A brief survey and an application of semantic image segmentation for autonomous driving, in: Handbook of Deep Learning Applications. Springer, pp. 161–200.
- Kliewer, W.M., Dokoozlian, N.K., 2005. Leaf area/crop weight ratios of grapevines: influence on fruit composition and wine quality. American Journal of Enology and Viticulture 56, 170–181.
- Kornblith, S., Shlens, J., Le, Q.V., 2019. Do better imagenet models transfer better?, in: Proceedings of the IEEE conference on computer vision and pattern recognition, pp. 2661–2671.
- Lampert, C.H., Blaschko, M.B., Hofmann, T., 2008. Beyond sliding windows: Object localization by efficient subwindow search, in: 2008 IEEE conference on computer vision and pattern recognition, IEEE. pp. 1–8.

- 918 Litjens, G., Kooi, T., Bejnordi, B.E., Setio, A.A.A., Ciompi, F., Ghafoorian,
919 M., Van Der Laak, J.A., Van Ginneken, B., Sánchez, C.I., 2017. A survey on
920 deep learning in medical image analysis. *Medical image analysis* 42, 60–88.
- 921 Long, J., Shelhamer, E., Darrell, T., 2015. Fully convolutional networks for
922 semantic segmentation, in: *Proceedings of the IEEE conference on computer*
923 *vision and pattern recognition*, pp. 3431–3440.
- 924 Lorenz, D., Eichhorn, K., Bleiholder, H., Klose, R., Meier, U., Weber, E., 1995.
925 Growth stages of the grapevine: Phenological growth stages of the grapevine
926 (*vitis vinifera* l. ssp. *vinifera*)—codes and descriptions according to the ex-
927 tended bbch scale. *Australian Journal of Grape and Wine Research* 1, 100–
928 103.
- 929 Lowe, D.G., 2004. Distinctive image features from scale-invariant keypoints.
930 *International journal of computer vision* 60, 91–110.
- 931 Matese, A., Di Gennaro, S.F., 2015. Technology in precision viticulture: A state
932 of the art review. *International journal of wine research* 7, 69–81.
- 933 May, P., 2000. From bud to berry, with special reference to inflorescence and
934 bunch morphology in *vitis vinifera* l. *Australian Journal of Grape and Wine*
935 *Research* 6, 82–98.
- 936 Moons, T., Van Gool, L., Vergauwen, M., 2009. 3D Reconstruction from Mul-
937 tiple Images: Principles. Now Publishers Inc.
- 938 Ning, C., Zhou, H., Song, Y., Tang, J., 2017. Inception single shot multibox
939 detector for object detection, in: *2017 IEEE International Conference on*
940 *Multimedia & Expo Workshops (ICMEW)*, IEEE. pp. 549–554.
- 941 Noyce, P.W., Steel, C.C., Harper, J.D., Wood, R.M., 2016. The basis of defolia-
942 tion effects on reproductive parameters in *vitis vinifera* l. cv. chardonnay lies
943 in the latent bud. *American Journal of Enology and Viticulture* 67, 199–205.
- 944 Nuske, S., Achar, S., Bates, T., Narasimhan, S., Singh, S., 2011. Yield estima-
945 tion in vineyards by visual grape detection, in: *2011 IEEE/RSJ International*
946 *Conference on Intelligent Robots and Systems*, IEEE. pp. 2352–2358.

947 Oguz, I., Carass, A., Pham, D.L., Roy, S., Subbana, N., Calabresi, P.A., Yushke-
948 vich, P.A., Shinohara, R.T., Prince, J.L., 2017. Dice overlap measures for
949 objects of unknown number: application to lesion segmentation, in: Interna-
950 tional MICCAI Brainlesion Workshop, Springer. pp. 3–14.

951 Pan, S.J., Yang, Q., 2009. A survey on transfer learning. *IEEE Transactions on*
952 *knowledge and data engineering* 22, 1345–1359.

953 Pérez, D.S., Bromberg, F., Diaz, C.A., 2017. Image classification for detection
954 of winter grapevine buds in natural conditions using scale-invariant features
955 transform, bag of features and support vector machines. *Computers and*
956 *electronics in agriculture* 135, 81–95.

957 Rowley, H.A., Baluja, S., Kanade, T., 1996. Human face detection in visual
958 scenes, in: *Advances in Neural Information Processing Systems*, pp. 875–881.

959 Rudolph, R., Herzog, K., Töpfer, R., Steinhage, V., 2018. Efficient identi-
960 fication, localization and quantification of grapevine inflorescences in un-
961 prepared field images using fully convolutional networks. *arXiv preprint*
962 *arXiv:1807.03770* .

963 Sánchez, L.A., Dokoozlian, N.K., 2005. Bud microclimate and fruitfulness in
964 *vitis vinifera* l. *American Journal of Enology and Viticulture* 56, 319–329.

965 Santos, T.T., de Souza, L.L., dos Santos, A.A., Avila, S., 2020. Grape detection,
966 segmentation, and tracking using deep neural networks and three-dimensional
967 association. *Computers and Electronics in Agriculture* 170, 105247.

968 Seng, K.P., Ang, L.M., Schmidtke, L.M., Rogiers, S.Y., 2018. Computer vision
969 and machine learning for viticulture technology. *IEEE Access* 6, 67494–67510.

970 Shelhamer, E., Long, J., Darrell, T., 2017. Fully convolutional networks for
971 semantic segmentation. *IEEE transactions on pattern analysis and machine*
972 *intelligence* 39, 640–651.

973 Shorten, C., Khoshgoftaar, T.M., 2019. A survey on image data augmentation
974 for deep learning. *Journal of Big Data* 6, 60.

975 Siam, M., Gamal, M., Abdel-Razek, M., Yogamani, S., Jagersand, M., 2018.
976 Rtseg: Real-time semantic segmentation comparative study, in: 2018 25th
977 IEEE International Conference on Image Processing (ICIP), IEEE. pp. 1603–
978 1607.

979 Simonyan, K., Zisserman, A., 2015. Very deep convolutional networks for large-
980 scale image recognition. CoRR abs/1409.1556.

981 Tardaguila, J., Diago, M., Blasco, J., Millán, B., Cubero, S., García-Navarrete,
982 O., Aleixos, N., 2012. Automatic estimation of the size and weight of
983 grapevine berries by image analysis, in: Proc. CIGR AgEng.

984 Tardáguila, J., Diago, M.P., Millan, B., Blasco, J., Cubero, S., Aleixos, N., 2012.
985 Applications of computer vision techniques in viticulture to assess canopy
986 features, cluster morphology and berry size, in: I International Workshop on
987 Vineyard Mechanization and Grape and Wine Quality 978, pp. 77–84.

988 Tarry, C., Wspanialy, P., Veres, M., Moussa, M., 2014. An integrated bud
989 detection and localization system for application in greenhouse automation,
990 in: 2014 Canadian Conference on Computer and Robot Vision, IEEE. pp.
991 344–348.

992 Tilgner, S., Wagner, D., Kalischewski, K., Velten, J., Kummert, A., 2019. Multi-
993 view fusion neural network with application in the manufacturing industry,
994 in: 2019 IEEE International Symposium on Circuits and Systems (ISCAS),
995 IEEE. pp. 1–5.

996 Vapnik, V., 2013. The nature of statistical learning theory. Springer science &
997 business media.

998 Wang, X., Han, T.X., Yan, S., 2009. An hog-lbp human detector with partial
999 occlusion handling, in: 2009 IEEE 12th international conference on computer
1000 vision, IEEE. pp. 32–39.

1001 Whalley, J., Shanmuganathan, S., 2013. Applications of image processing in
1002 viticulture: A review .

- 1003 Whelan, B., McBratney, A., Viscarra Rossel, R., 1996. Spatial prediction for
1004 precision agriculture, in: Proceedings of the Third International Conference
1005 on Precision Agriculture, Wiley Online Library. pp. 331–342.
- 1006 Xu, S., Xun, Y., Jia, T., Yang, Q., 2014. Detection method for the buds
1007 on winter vines based on computer vision, in: 2014 Seventh International
1008 Symposium on Computational Intelligence and Design, IEEE. pp. 44–48.
- 1009 Zhao, F., Rong, D., Liping, L., Chenlong, L., 2018. Research on stalk crops
1010 internodes and buds identification based on computer vision. MS&E 439,
1011 032080.